

# Twisted MoSe<sub>2</sub> Bilayers with Variable Local Stacking and Interlayer Coupling Revealed by Low-Frequency Raman Spectroscopy

Alexander A. Puretzy,<sup>\*,†,⊥</sup> Liangbo Liang,<sup>†,⊥</sup> Xufan Li,<sup>†</sup> Kai Xiao,<sup>†</sup> Bobby G. Sumpter,<sup>†,§</sup> Vincent Meunier,<sup>‡</sup> and David B. Geohegan<sup>†</sup>

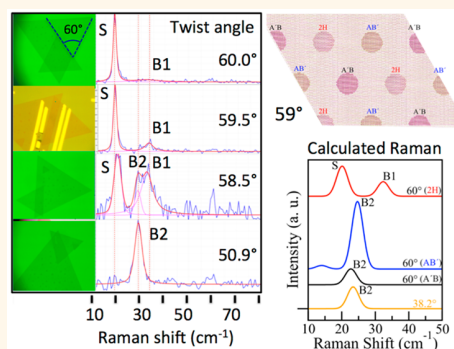
<sup>†</sup>Center for Nanophase Materials Sciences and <sup>§</sup>Computer Science and Mathematics Division, Oak Ridge National Laboratory, Oak Ridge, Tennessee 37831, United States

<sup>‡</sup>Department of Physics, Applied Physics, and Astronomy, Rensselaer Polytechnic Institute, Troy, New York 12180, United States

## Supporting Information

**ABSTRACT:** Unique twisted bilayers of MoSe<sub>2</sub> with multiple stacking orientations and interlayer couplings in the narrow range of twist angles,  $60 \pm 3^\circ$ , are revealed by low-frequency Raman spectroscopy and theoretical analysis. The slight deviation from  $60^\circ$  allows the concomitant presence of patches featuring all three high-symmetry stacking configurations (2H or AA', AB', and A'B) in one unique bilayer system. In this case, the periodic arrangement of the patches and their size strongly depend on the twist angle. *Ab initio* modeling predicts significant changes in frequencies and intensities of low-frequency modes versus stacking and twist angle. Experimentally, the variable stacking and coupling across the interface are revealed by the appearance of two breathing modes, corresponding to the mixture of the high-symmetry stacking configurations and unaligned regions of monolayers. Only one breathing mode is observed outside the narrow range of twist angles. This indicates a stacking transition to unaligned monolayers with mismatched atom registry without the in-plane restoring force required to generate a shear mode. The variable interlayer coupling and spacing in transition metal dichalcogenide bilayers revealed in this study may provide an interesting platform for optoelectronic applications of these materials.

**KEYWORDS:** two-dimensional materials, transition metal dichalcogenides, low-frequency Raman spectroscopy, stacking configurations, first-principles calculations



The fundamental properties and potential applications of artificially structured van der Waals materials constructed by stacking two-dimensional crystalline monolayer “building blocks” have recently attracted the attention of many researchers.<sup>1</sup> In particular, an intense exploration of the optoelectronic properties of transition metal dichalcogenide (TMD) bilayer heterostructures has revealed many interesting phenomena including extremely fast and efficient interlayer charge<sup>2–4</sup> and energy<sup>5,6</sup> transfer, interlayer excitons,<sup>7,8</sup> and new emerging properties of atomically thin p–n junctions.<sup>9,10</sup> Controlling the assembly of these vertically stacked 2D crystals to ensure a well-defined mutual orientation and a clean atomically sharp interface remains a major challenge in the practical fabrication of these structures. Although bilayers of 2D crystals can be synthesized directly by chemical vapor deposition (CVD)<sup>6,11</sup> with a limited number of possible phases (i.e., stacking configurations), the stamping approach can assemble CVD-grown<sup>2,12–14</sup> or exfoliated<sup>3,4,7,8,10</sup> 2D monolayers with a theoretically infinite variety of possible

stacking patterns. Understanding how interlayer forces resulting from atomistic interactions, not only drive the alignment, but also determine the optoelectronic properties of bilayers, is essential to developing assembly and characterization approaches for the fast and effective selection and exploration of artificially stacked 2D crystals.

Optical spectroscopies including photoluminescence,<sup>15</sup> absorption,<sup>6</sup> second-harmonic generation,<sup>16,17</sup> and Raman scattering<sup>18–20</sup> have been used to characterize stacked 2D crystals. Among these approaches, low-frequency (LF) Raman spectroscopy is the most sensitive technique to probe van der Waals interlayer coupling because it can detect the in-plane shear and out-of-plane breathing vibrations of entire 2D layers.<sup>21–25</sup>

LF Raman spectroscopy has been very successful in characterizing the thickness-dependent interlayer interactions

**Received:** December 11, 2015

**Accepted:** January 12, 2016

**Published:** January 14, 2016

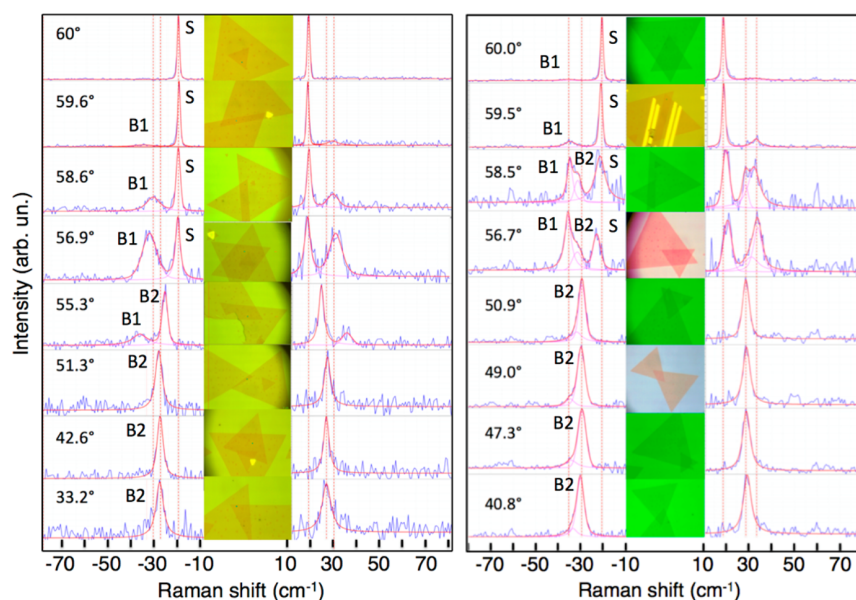


**Figure 1.** (Left panel) Set of Stokes and anti-Stokes Raman spectra measured at different twist angles from  $60^\circ$  to  $33.2^\circ$  at room temperature for bilayers of  $\text{MoSe}_2$  (blue lines). Note that the upper spectra at a  $60^\circ$  twist angle were measured using as-grown  $\text{MoSe}_2$  bilayers in the 2H stacking configuration. The vertical dotted lines show the positions of the shear Raman peak disappearing at  $\leq 55.3^\circ$  twist angles and the emerging peaks corresponding to two breathing modes. (Right panel) Set of Stokes and anti-Stokes Raman spectra measured at room temperature for different twist angles ranging from  $60^\circ$  to  $40.8^\circ$  for a bilayer  $\text{MoSe}_2$  sample doped with W (blue lines). The vertical dotted lines show the positions of the shear Raman peak that disappears at twist angles of  $< 56.7^\circ$  and the appearance of new peaks corresponding to two breathing modes. Note that the upper spectra at a  $60^\circ$  twist angle were acquired using artificially stacked monolayers. For both panels the central columns show optical images of the bilayers used to determine the twist angles and the red lines indicate fitting using Voigt profiles without fixing any of the peak positions or peak widths. Here S, B1, and B2 mark shear and two breathing modes, respectively. The three-peak fit to deconvolute B1 and B2 was used only in the case of a clear and reproducible shoulder corresponding to the B2 mode. All spectra were acquired under a parallel,  $z(x,x)\bar{z}$ , polarization configuration.

and number of layers in diverse 2D layered materials, such as graphene,<sup>26–28</sup> TMDs,<sup>21–24</sup> black phosphorus,<sup>29,30</sup>  $\text{ReSe}_2$ ,<sup>31</sup>  $\text{ReS}_2$ ,<sup>32</sup> and  $\text{Bi}_2\text{Te}_3$  and  $\text{Bi}_2\text{Se}_3$ .<sup>33</sup> In addition, LF Raman spectroscopy has also been recently used to reveal the relationship between interfacial coupling and stacking pattern in twisted multilayer graphene.<sup>26,34,35</sup> Furthermore, in a recent work we showed that the most stable stacking configurations, 2H (or AA') and 3R (or AB), in bilayers and even more complex 2H-2H, 2H-3R, and 3R-3R stackings in trilayers of  $\text{MoSe}_2$  can be identified using LF Raman scattering.<sup>18</sup> In that study we demonstrated how LF Raman fingerprints could decode the stacking configurations within multiple regions of a complex crystal consisting of 1L–3L  $\text{MoSe}_2$ . In that particular work, the triangular 2D TMD crystals synthesized by CVD exhibited only the most stable 2H and 3R stacking configurations in bilayers, corresponding to mutual twist angles between the triangles of  $60^\circ$  and  $0^\circ$ , respectively.<sup>18</sup> The importance of this approach to decode layer stacking was also emphasized recently for stacked TMDs monolayers<sup>20,36,37</sup> and  $\text{ReS}_2$ .<sup>32</sup>

The complexity introduced by artificially stacking 2D TMD bilayers with arbitrary twist angle between  $0^\circ$  and  $60^\circ$  raises a number of fundamental questions. How does interlayer coupling depend on the twist angle? How do the frequencies and Raman intensities of the LF shear and breathing modes evolve with the twist angle? Are there any characteristic features in the LF Raman spectra that can be used to characterize interlayer coupling? Addressing these questions is important for a fundamental understanding of van der Waals 2D interlayer

interactions as well as for the development of simple and effective characterization of artificially stacked 2D materials.

Initial LF Raman spectroscopy studies of TMD bilayers showed high sensitivity of the LF modes to the details of the interface, as revealed by observation of the breathing mode corresponding to vibrations between incommensurate monolayers.<sup>19</sup> However, large uncertainty in the mutual rotational angles ( $< 5^\circ$ ) between TMD monolayers in the work of ref 19 did not allow study of the most interesting transitional orientations with twist angles close (but not equal) to  $0^\circ$  and  $60^\circ$  where lattice registry exhibits coexisting commensurate and incommensurate bilayer stacking. Furthermore, first-principles theory has not been used to reveal the microscopic picture of the stacking and LF Raman evolution versus the twist angle in TMD bilayers.

Here we report results of LF Raman scattering in bilayers of  $\text{MoSe}_2$  prepared using the wet transfer method from CVD-grown monolayers with a wide variety of twist angles. The high quality of the transferred monolayer crystals permits determination of the twist angles with an uncertainty of  $\pm 0.5^\circ$  using optical imaging, which allows us to monitor evolution of the LF shear and breathing modes in the transient region between commensurate and incommensurate  $\text{MoSe}_2$  lattice registries, close to a  $60^\circ$  twist angle. Upon only slight detuning ( $\sim 0.5^\circ$ ) from the  $60^\circ$  2H stacking configuration, we observe that the extremely weak and broad breathing mode<sup>18</sup> becomes much more pronounced and also that the shear mode rapidly disappears as the lateral restoring force between the layers is reduced as stacking becomes unaligned with mismatched periodicity.<sup>28</sup> Within the narrow range of twist angles from

60° to 57°, theoretical predictions of the coexistence of different high-symmetry stacking patches, and the two breathing modes and one shear mode predicted for the Raman spectra, were experimentally confirmed.

## RESULTS AND DISCUSSION

**MoSe<sub>2</sub> Sample Characterization.** Stacked bilayers of MoSe<sub>2</sub> crystals with arbitrary interlayer rotation angles were assembled from CVD-grown monolayers by transferring the MoSe<sub>2</sub> monolayers from one SiO<sub>2</sub>/Si substrate and stacking them onto the as-grown MoSe<sub>2</sub> monolayers on another substrate. The detailed procedure is described in the [Methods](#) section. The crucial aspect of the as-synthesized and transferred MoSe<sub>2</sub> crystals is their perfect equilateral triangular shape that allows precise measurements of the twist angles using optical imaging. Figure S1 in the [Supporting Information](#) (SI) shows an optical microscope image of a typical MoSe<sub>2</sub> bilayer crystal that demonstrates a perfect equilateral triangular shape of its as-grown and stacked monolayer components with all three angles equal to 60 ± 0.5°.

Another important procedure in fabrication of bilayers using the transfer approach (see [Methods](#) section for details) is the proper annealing of the artificially stacked samples, since without annealing, the LF Raman lines are not observable. We note, however, the high-frequency (HF) Raman spectra do not show any significant changes upon annealing (a schematic of vibrations for LF and HF Raman modes is shown in Figure S2 in the SI). Furthermore, it should be mentioned that the thermal treatment introduces some imperfections and wrinkles in the overlapped regions, as can be seen from atomic force microscopy (AFM) images of the MoSe<sub>2</sub> crystals (Figures S3, S4 in the SI). The AFM images show that as-grown mono- and bilayers (red profile, Figure S3) as well as the nonoverlapping part of the transferred monolayer are clean, but the overlapping region that forms the twisted bilayer exhibits multiple wrinkles and imperfections (blue profiles with multiple spikes in Figures S3 and S4). The same behavior of the overlapped regions has been noticed previously in the case of MoS<sub>2</sub>/WSe<sub>2</sub> heterobilayers fabricated using a similar procedure.<sup>13</sup> Despite the wrinkles and imperfections, the bilayer Raman spectra measured from different spots within the same bilayer are found to be very reproducible (see, for example, Figure S5). Since wrinkles and imperfections might affect the Raman spectra and their twist angle dependence, we used two samples synthesized and processed using slightly different conditions (see [Methods](#) section) and performed a detailed comparative analysis of the twist angle dependence for both samples.

**Raman Spectra of Twisted MoSe<sub>2</sub> Bilayers.** Figure 1 (left panel) shows a set of Stokes and anti-Stokes LF Raman spectra measured for a number of samples with different twist angles in the range extending from 60° to 33.2°. Note that in this case the spectra for the 60° twist angle were measured using as-grown MoSe<sub>2</sub> bilayers. This system is found in the natural 2H stacking configuration and shows only the shear mode at 19.2 cm<sup>-1</sup> (see also ref 18). One can see that even slight deviation from 60° (spectra at 59.6° angle) results in the appearance of the breathing mode, B<sub>1</sub>, at 32.3 cm<sup>-1</sup>. The intensity of this mode increases until it reaches the intensity of the shear mode at the twist angle of 56.9°. At a 55.3° twist angle the LF Raman spectra change drastically; that is, the shear mode disappears leaving two shifted peaks corresponding to the breathing modes, B<sub>1</sub> and B<sub>2</sub>, as confirmed by polarized Raman measurements (see Figure S6 in the SI). Further decrease of

the twist angle to 51.3° leads to a single breathing mode peak, B<sub>2</sub>, located at 27.0 cm<sup>-1</sup> with a full width at half-maximum (fwhm) of 3.6 cm<sup>-1</sup>. More detailed analysis of the breathing mode shape in the narrow range of twist angles between 57° and 55° (Figure 2) shows the clear appearance of a new peak,

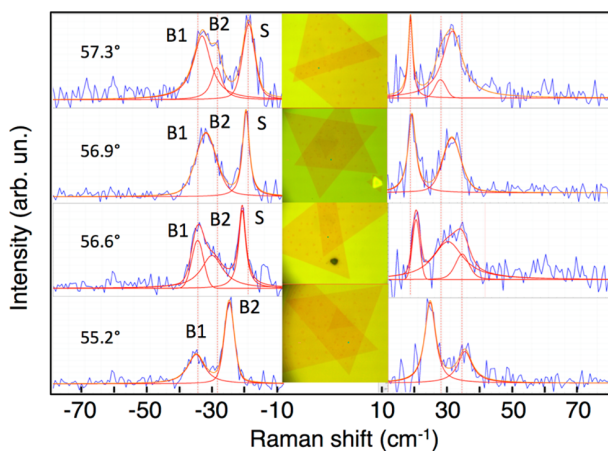


**Figure 2.** Set of Stokes and anti-Stokes Raman spectra measured at twist angles ranging from 57.3° to 55.2° under a parallel,  $z(x,x)\bar{z}$ , laser polarization configuration (blue lines). Here S, B<sub>1</sub>, and B<sub>2</sub> mark shear and two breathing modes, respectively. The red lines show the result of fitting using Voigt profiles without fixing any of the peak positions or peak widths. The three-peak fit to deconvolute B<sub>1</sub> and B<sub>2</sub> was used only in the case of a clear and reproducible shoulder corresponding to the B<sub>2</sub> mode. Note that at the twist angles of  $\leq 55.2^\circ$  the 19.2 cm<sup>-1</sup> shear mode disappears. The central column shows optical images of the bilayers used to determine the twist angles. The Raman spectra correspond to the first sample (left panel, Figure 1).

B<sub>2</sub>, located between the shear and breathing (B<sub>1</sub>) Raman lines that becomes the major feature of the LF Raman spectrum at a twist angle of 55.2°. Since both peaks at a 55.2° twist angle disappear under the backscattering  $z(x,y)\bar{z}$  polarization configuration<sup>23</sup> (see Figure S6 in the SI), they can both be attributed to the breathing modes, B<sub>1</sub> and B<sub>2</sub>.

The second sample shows very similar evolution of the LF Raman spectra *versus* twist angle (Figure 1, right panel). Note that in this case we were able to find an artificial stacking with a 60.0 ± 0.5° twist angle and compare its LF Raman spectra with those measured for as-grown bilayers at 60° twist angle (right and left upper rows in Figure 1, respectively). This comparison shows that the spectra are almost identical, with only a slightly more pronounced breathing mode feature at 34 cm<sup>-1</sup> in the case of artificially stacked monolayers (right upper panel). At 58.5° and 56.7° twist angles one can clearly see the emergence of the second breathing mode, B<sub>2</sub>, which appears as a shoulder flanked to the left (right) of the original breathing mode, B<sub>1</sub>, for Stokes (anti-Stokes) spectra. The B<sub>2</sub> mode remains the only feature in the LF Raman spectra at twist angles of  $\leq 50.9^\circ$ .

Figure 3 summarizes our results on the Raman shifts and peak intensities of the shear and breathing modes *versus* twist angles for sample 1 (Figure 1, left panel). First, one can clearly see a sharp drop of the shear mode peak intensity with only slight deviations from the 60° configuration (Figure 3d). Only very small variation ( $\sim 0.5$  cm<sup>-1</sup>) of its frequency is observed within the observation region marked by the vertical dotted lines in Figure 3b. Note that outside the observation region the

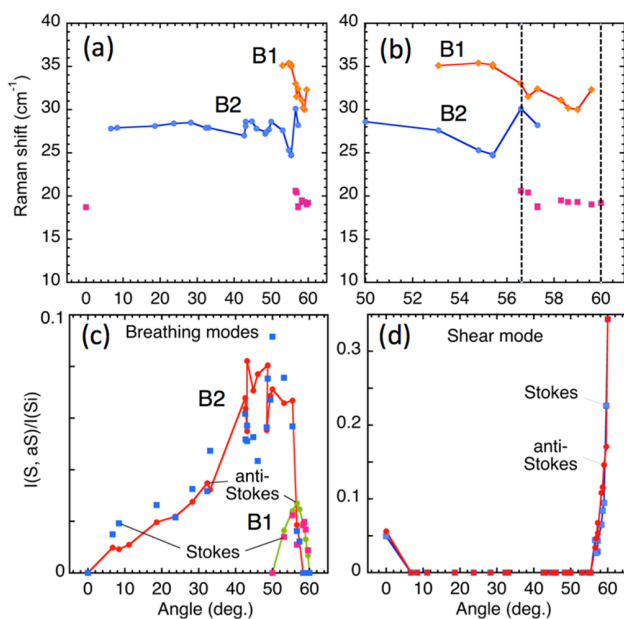


**Figure 3.** (a) Measured Raman shifts of the shear and two breathing modes,  $B_1$  and  $B_2$ , versus a twist angle between two  $\text{MoSe}_2$  monolayers; (b) the enlarged region around  $60^\circ$ . The vertical dashed lines mark the twist angle region where the shear Raman line is observed. (c, d) Peak intensities of two breathing,  $B_1$  and  $B_2$  (c), and one shear (d) Raman line normalized to the peak intensity of the  $521\text{ cm}^{-1}$  Si line in Stokes and anti-Stokes spectral regions versus a twist angle. Note that the Si substrate was properly oriented relative to the polarization direction of the incident laser light to maximize the intensity of the  $521\text{ cm}^{-1}$  Si peak and that this orientation was maintained for all measurements.

shear mode peak disappears, largely due to its almost zero frequency since the in-plane shear vibrations lead to virtually no restoring force from the unaligned stacking. This mismatched stacking is characterized by the lack of any local high-symmetry arrangements between monolayers at these twist angles,<sup>19,35</sup> as confirmed by the first-principles calculations discussed below. In the region of the twist angles where the shear mode still exists (Figure 3d) we also observe a slight increase of the breathing mode frequency when the twist angle decreases and the sharp emergence of a new breathing mode,  $B_2$ , with lower frequency. The frequency of the new breathing mode,  $B_2$ , remains constant within the broad range of the twist angles from  $8^\circ$  to  $50^\circ$  (Figure 3a); however its peak intensity drops at the smaller angles, making its detection difficult (Figure 3c). Interestingly, the intensity of the original breathing mode,  $B_1$ , initially rapidly increases and then drops to zero within only  $10^\circ$  from the  $60^\circ$  twist angle of the most stable 2H configuration.

The frequency of the high-frequency Raman mode,  $A_{1g}$  (Figure S2), for this sample does not show any significant dependence on the twist angle, as it remains constant within  $241 \pm 0.5\text{ cm}^{-1}$  except for one data point at  $242.0\text{ cm}^{-1}$ , corresponding to the 3R ( $0^\circ$ ) stacking configuration (Figure S7b). However, the peak intensity of this mode is slightly higher ( $\sim 1.5$  times) in the range of twist angles from  $20^\circ$  to  $50^\circ$  compared to that in the range from  $0^\circ$  to  $10^\circ$  (see Figure S7c). Nevertheless, compared to the LF Raman modes, the HF mode shows much fewer frequency and intensity variations with the twist angle, confirming that the LF modes are more sensitive to interlayer stacking and coupling.<sup>18</sup>

To understand the possible effects of bilayer sample quality on the observed LF Raman spectra, including defects, wrinkles, and other imperfections that might have been introduced

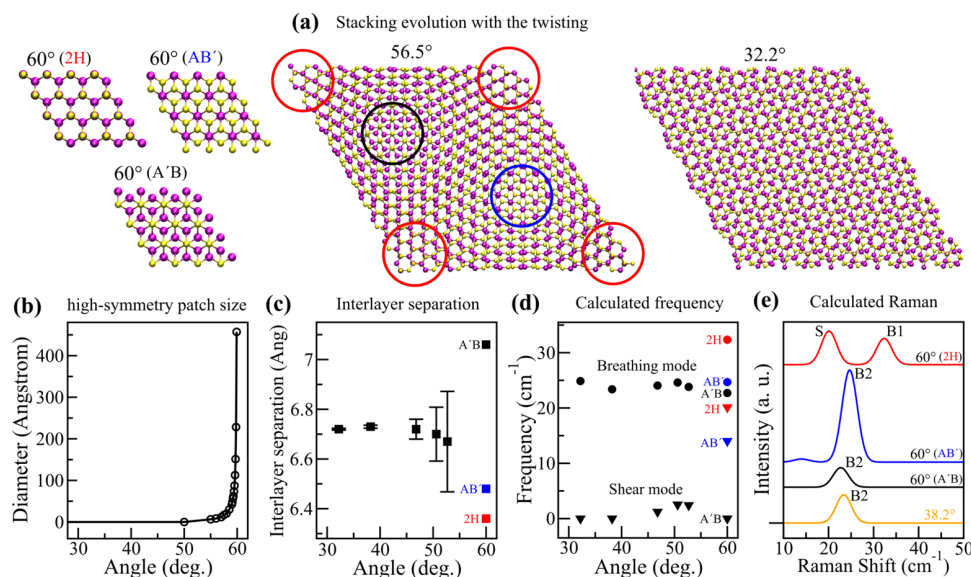


**Figure 4.** Results of DFT calculations at different twist angles. (a) Atomic structures of commensurate bilayer  $\text{MoSe}_2$ . At  $60^\circ$ , there are three high-symmetry stacking patterns, 2H,  $AB'$ , and  $A'B$ . They coexist as patches in the stacking near  $60^\circ$  (highlighted by circles of different colors at  $56.5^\circ$ ). The patch diameters continuously decrease with deviation from  $60^\circ$ , and the stacking becomes completely unaligned near  $30^\circ$ . (b) Diameter of the high-symmetry stacking patches versus the twist angle. (c) Average interlayer distance between the two Mo layers. (d) Calculated frequencies of low-frequency shear mode (triangle) and breathing mode (circle). In (c) and (d), all three stackings 2H,  $AB'$ , and  $A'B$  are considered at  $60^\circ$  (hence three data points at  $60^\circ$  as distinguished by colors and labels). (e) Simulated low-frequency Raman spectra of the three high-symmetry stackings at  $60^\circ$  and unaligned stacking at  $38.2^\circ$ . The shear mode peak is labeled as S, while the breathing mode peak is labeled as  $B_1$  or  $B_2$  depending on the position. More details are provided in Figures S14 and S15 and Table S1.

during the growth of MoSe<sub>2</sub> monolayers, stacking into bilayers, and annealing, we conducted similar twist angle dependence measurements using the second MoSe<sub>2</sub> bilayer sample (Figure 1, right panel). This bilayer sample was slightly doped with W (a few atomic %, equally distributed between bottom and top monolayers). The presence of dopant does not affect the LF Raman spectra, but allows us to synthesize better quality samples.<sup>18</sup> The dependence of the shear and breathing modes' Raman shifts (Figure S8) and the peak intensities (Figures S9, S10) are also very similar to that shown in Figure 3. Figure S11 in the SI shows direct comparison of the twist angle evolution of the Raman shifts for these two samples.

**Modeling of Raman Spectra.** The observed changes in LF Raman spectra are likely due to variations in interlayer stacking and coupling induced by twisting. To verify this hypothesis, we carried out first-principles density functional theory (DFT) calculations for various stacking configurations and twist angles. Here we focus on the twist angles from 60° to 30°, as they are of most interest for comparison with experimental results. As shown in Figure 4a and Figure S12, at 60°, there are three high-symmetry stacking patterns, 2H, AB', and A'B: for 2H (also denoted as AA'), Mo of layer 1 are over Se of layer 2 and Se of layer 1 are over Mo of layer 2; for AB', Mo (layer 1) are over Mo (layer 2) and all Se (layer 1) are over the center of the hexagons (layer 2); for A'B, Se (layer 1) are over Se (layer 2) and all Mo (layer 1) are over the center of the hexagons (layer 2).<sup>38–40</sup> They can be translated into one another by simple in-plane shifts. Slightly detuning from 60° to 56.5°, 2H, AB', and A'B stacking patches all show up in the stacking configuration, as highlighted by the red, blue, and black circles in Figure 4a, respectively. The patch sizes continuously decrease with twist angle  $\theta$  deviating from 60°, and eventually the stacking becomes completely unaligned at 32.2° in Figure 4a (additional examples with twist angles including 58.2°, 52.7°, 46.8°, and 38.2° are shown in Figures S13 and S14). We also consider noncommensurate finite-size bilayer systems in Figure S15. Similar to Figure 4a, when the system slightly deviates from 60°, all three stacking configurations 2H, AB', and A'B appear in similar roughly circular shapes. These moiré-like circular high-symmetry stacking patches are clearly periodic like the triangular lattice. The diameters of the circular patches at each angle were estimated and are shown in Figure 4b. Clearly, their sizes continuously decrease with the twist angle,  $\theta$ , deviating from 60°. When  $\theta < 55^\circ$ , one can see the stacking transfer from a mixture of multiple high-symmetry stacking configurations to an increasingly mismatched atomic alignment (Figure S15).

*Ab initio* calculations for angles of 32.2°, 38.2°, 46.8°, 50.6°, 52.7°, and 60° (three stackings 2H, AB', and A'B) are shown in Figure 4 and Table S1. Unfortunately, calculations of angles closer to 60° (such as 56.5° or 58.2°) are computationally very difficult, as the number of atoms in the unit cell exceeds 1500. However, the theoretical results available for more modest unit cell sizes can provide significant insight in the overall evolution of the Raman spectra. We first examine the three high-symmetry stackings at 60°. Moving from 2H to AB' to A'B stacking is characterized by an increasing interlayer distance, a reduced thermodynamic stability, and a weakening interlayer coupling strength (Figure 4c and Table S1). For the shear mode, both frequency and intensity decrease significantly (Figure 4d,e and Table S1). For the breathing mode, the frequency also decreases notably, but not as dramatically as for the shear mode (Figure 4d,e and Table S1). More interestingly, in contrast to the shear mode, the intensity of the breathing

mode increases considerably from 2H to AB' stacking, while it slightly increases from 2H to A'B stacking. Such intensity increase of the breathing mode by changing stacking has been recently experimentally observed in bilayer WSe<sub>2</sub> and was ascribed to a change in symmetry.<sup>18</sup> In short, there are two distinctive breathing mode peaks among 2H, AB', and A'B stackings at 60° for bilayer MoSe<sub>2</sub>: B<sub>1</sub> for 2H stacking with higher frequency; B<sub>2</sub> for AB' and A'B stackings with similar lower frequency (Figure 4e). On the other hand, the shear mode peak is too weak for AB' and A'B stackings (Figure 4e).

For other angles including 52.7°, 50.6°, 46.8°, 38.2°, and 32.2°, the high-symmetry stacking patches disappear, and the overall stacking shows less and less local order resembling any of the high-symmetry patches discussed above. At these angles, the calculated average interlayer distance is about the same, and thus interlayer coupling is of similar magnitude (Figure 4c and Table S1). Hence, the breathing mode is located around 24 cm<sup>-1</sup> with minor variations, similar to the values for AB' and A'B stackings (Figure 4d). However, it is smaller than that of 2H stacking because the interlayer distance is larger. Interestingly, in contrast with the breathing mode, the shear mode shows an extremely low frequency at these angles (Figure 4d). This can be attributed to the unaligned stacking without an in-plane restoring force. For the unaligned stacking pattern like that at 32.2° shown in Figure 4a, the in-plane shear motion only slightly changes the relative layer–layer stacking and gives very small overall restoring force, while the out-of-plane breathing motion changes the interlayer distance and coupling and thus always leads to a finite overall restoring force.<sup>19,37</sup> In addition, we computed the Raman intensities for the 38.2° twist angle (Figure 4e and Table S1), as it has the smallest unit cell with 42 atoms among all considered twist angles  $\theta \neq 60^\circ$  and is still computationally affordable. The shear mode peak is invisible due to the nearly zero frequency, while the breathing mode peak shows comparable intensity to that of 2H or A'B stacking, suggesting that the breathing vibration of the unaligned MoSe<sub>2</sub> bilayer still leads to notable signal.

Such unique stacking dependence of LF Raman spectra revealed by simulations can explain many features of the experimentally observed evolution of the LF Raman spectra. First, as discussed above, stacking at  $\theta > 55^\circ$  features a mixture of high-symmetry stacking patches 2H, AB', and A'B, and thus the overall Raman scattering is expected to feature a combination of Raman signature of the 2H, AB', and A'B patterns as well. This explains the experimental observation of two breathing modes, B<sub>1</sub> and B<sub>2</sub>, where the higher frequency mode B<sub>1</sub> corresponds to the most stable 2H patch and the lower frequency mode B<sub>2</sub> probably comes from less stable AB' and A'B patches (Figures 2, 3a–c, 4e, and S8–11). Second, the shear mode exhibits too low frequency and intensities for AB' and A'B patches and hence is practically invisible, which explains why only one shear mode is experimentally observed at  $\theta > 55^\circ$ , coming from the 2H patch (Figure 4e). As the patch size decreases exponentially with  $\theta$  detuning from 60°, the shear mode intensity has a sharp drop (Figure 3d). Third, for  $\theta < 55^\circ$ , since the 2H patch begins to disappear, the B<sub>1</sub> mode also disappears, as observed experimentally (Figure 3c). Although the AB' and A'B patches diminish as well, since the mismatched stacking yields a B<sub>2</sub> peak at a similar position (Figure 4e), the B<sub>2</sub> peak is always present for any twist angle. In the wide range of twist angles between 5° and 55°, as the interlayer coupling varies little according to calculations (Figure 4c,d and Table S1), the measured frequency of B<sub>2</sub> generally

changes little (Figure 3a). The notable frequency change occurs around  $55^\circ$ , correlating with the stacking transition from high-symmetry patches to mismatched atomic alignment. Furthermore, the unaligned stacking eliminates the restoring force required for generation of a shear mode. Consequently, for  $\theta < 55^\circ$ , we observed a rather simple LF Raman spectrum that consists of a single Raman line corresponding to the breathing mode  $B_2$  (Figures 1, 3a–c, and 4e).

Another interesting observation is the emergence of the breathing mode with only slight deviations ( $0.5^\circ$ ) from the  $60^\circ$  (2H) stacking configuration, where this mode is not observable. As we pointed out earlier, a possible explanation of this effect is the strong anharmonic coupling of the breathing mode with other low-frequency modes.<sup>18</sup> The anharmonic coupling between breathing, shear, and acoustic modes has also been suggested as the primary effect leading to broadening of the breathing mode in few layered  $\text{MoS}_2$ .<sup>41</sup> Here we observed that even a slight deviation from the stable 2H configuration results in efficient decoupling of the LF modes and emergence of the breathing mode,  $B_1$ . Further decrease of a twist angle leads to the disappearance of  $B_1$  due to a sharp decrease of the 2H patch sizes (Figure 4b). However, understanding this process requires the development of first-principles anharmonic models,<sup>42</sup> which to our knowledge has not been done yet for TMDs. Another important point is the resonant character of Raman scattering in TMDs that also can result in redistribution of intensities between LF modes with different symmetries.

## CONCLUSIONS

In summary, low-frequency Raman measurements and modeling of twisted  $\text{MoSe}_2$  bilayers revealed variable interlayer stacking and coupling in a narrow range of relative twist angles ( $\pm 3^\circ$ ) around  $60^\circ$ . This slight deviation from  $60^\circ$  results in the coexistence of localized patches of all three high-symmetry stacking configurations (2H,  $AB'$ ,  $A'B$ ). The periodic arrangement of the patches and their size strongly depend on the twist angle, leading to variations in coupling strength. The periodically variable van der Waals coupling across the interface results in the appearance of two breathing modes that correspond to the moiré supercells with 2H stacking and the other two high-symmetry stackings and possibly unaligned regions of bilayers. The unaligned regions with the mismatched registry between atoms in monolayers grow rapidly with decreasing twist angle at the expense of the high-symmetry stacking regions, which results in the disappearance of the shear mode and emergence of a single breathing mode corresponding to this mismatched alignment.

The evolution of the interlayer coupling with the twist angle manifests itself in characteristic changes in the LF Raman frequencies and intensities in the narrow range of the twist angles around  $60^\circ$ , *i.e.*, a sharp drop of the shear mode intensity and increase of the new lower breathing mode intensity that appears at the lower frequencies relative to the original breathing mode from the 2H stacking configuration. The characteristic changes in the intensities of the LF Raman peaks and their frequencies can be used for characterization of the interlayer coupling, *e.g.*, for determination of the existence of the high-symmetry commensurate regions in the unaligned stacking configurations in TMDs.

According to our calculations, the three high-symmetry stacking patches together with unaligned regions of monolayers should emerge in a bilayer near  $60^\circ$  twist angle for any TMD with the monolayers' symmetry the same as in the  $\text{MoSe}_2$  case

considered here. Therefore, all TMD bilayers with monolayers belonging to the same noncentrosymmetric  $D_{3h}$  point group should exhibit similar evolution of low-frequency modes near  $60^\circ$ .

Our results and further development of LF Raman spectroscopy of layered 2D materials together with first-principles modeling provide a new understanding of interlayer stacking and coupling, which is crucial for designing new artificially layered materials with different functionalities. We note that the observed evolution of the Raman lines corresponding to breathing modes is very important for understanding the strong anharmonic coupling between LF modes. Phonon–phonon interaction is the major mechanism that determines thermal transport in few-layer TMDs, and further understanding of anharmonic coupling and development of an *ab initio* anharmonic model will be important to achieve additional progress in this field.

## METHODS

**CVD Growth of  $\text{MoSe}_2$  Monolayer Crystals.** The CVD growth procedure was described in detail in our previous paper (see ref 18). Briefly, monolayer  $\text{MoSe}_2$  and W-doped  $\text{MoSe}_2$  crystals were synthesized in a CVD setup at  $780^\circ\text{C}$ . First, Si substrates with a 250 nm  $\text{SiO}_2$  layer were cleaned using acetone and 2-propanol and then placed onto an alumina boat with 0.25 g of  $\text{MoO}_3$  powder (0.20 g of  $\text{MoO}_3$  and 0.20 g of  $\text{WO}_3$  in the case of the second sample, W-doped  $\text{MoSe}_2$ ) that was positioned at the center of the CVD reactor. Another alumina boat containing 1.2 g of Se powder was inserted into the upstream side of the CVD reactor. The CVD reactor was pumped down to  $\sim 5$  mTorr, and the flow of the carrier gas (40 sccm (standard cubic centimeters per minute) Ar and 4 sccm  $\text{H}_2$ ) was established in the reactor. The synthesis was performed at  $780^\circ\text{C}$  ( $30^\circ\text{C}/\text{min}$  temperature ramping rate) for 5 min at the total pressure of 20 Torr. At the location of the Se powder boat the temperature was maintained at  $290^\circ\text{C}$ .

**Fabrication of Twisted Bilayers.** To fabricate twisted stacked bilayers of  $\text{MoSe}_2$ , the  $\text{SiO}_2/\text{Si}$  substrate with as-grown monolayer  $\text{MoSe}_2$  crystals was cut into two parts, one of which was coated with poly(methyl methacrylate) (PMMA) by spinning at 3500 rpm (revolutions per min) for 1 min followed by removing the  $\text{SiO}_2$  epilayer that was performed using etching in 1.5 M KOH solution in a Petri dish at  $80^\circ\text{C}$ . As a result of this procedure, we obtained a free-floating PMMA film with the  $\text{MoSe}_2$  monolayer crystals on the solution surface. The film was transferred to another beaker with deionized water by scooping it with a thin glass slide and was kept there for 10 min to remove residual KOH solution. This water rinsing procedure was repeated three times. After this bilayers of  $\text{MoSe}_2$  crystals were fabricated by stacking the free PMMA/ $\text{MoSe}_2$  films on the second half of the  $\text{SiO}_2/\text{Si}$  substrate with the as-grown monolayer  $\text{MoSe}_2$  crystals. To do this, the second half of the  $\text{SiO}_2/\text{Si}$  substrate with  $\text{MoSe}_2$  monolayer crystals was put into a funnel filled with deionized water followed by transfer of the floating PMMA/ $\text{MoSe}_2$  film from a beaker with water to the funnel using a glass slide. Then water was slowly drained from the funnel, forcing the floating film to go down and finally get stuck onto the second half of the substrate at the bottom of the funnel. This step is the key procedure to obtain intact transferred  $\text{MoSe}_2$  crystals with perfect equilateral triangular shape required for our study. Finally, the PMMA film was removed with acetone followed by annealing at  $300^\circ\text{C}$  in flowing Ar (95%)/ $\text{H}_2$  (5%) at atmospheric pressure for 2 h. Note that without annealing we did not observe any LF Raman lines. The same procedure was used to prepare the second twisted bilayer sample with equally doped bottom and top monolayers (a few atomic %) since they originated from the same substrate with as-grown W-doped  $\text{MoSe}_2$  monolayers.

**Raman Measurements.** The detailed description of our Raman setup is given in ref 18. Briefly, the measurements were performed using a micro-Raman setup (T64000 triple spectrometer, Jobin-Yvon) equipped with three 1800 grooves per millimeter gratings (spectral

resolution  $\sim 0.7 \text{ cm}^{-1}$ , fwhm) and a liquid nitrogen cooled CCD (Symphony, Horiba JY). All measurements were performed at room temperature under a microscope in the backscattering configuration using a 532 nm excitation laser. The linearly polarized laser beam was focused on a sample surface to a  $\sim 1 \mu\text{m}$  spot using a 100 $\times$  objective (NA = 0.9) with the typical laser power on the samples being  $\sim 0.3$  mW. To get a sufficient signal-to-noise ratio, 1–5 min acquisition times were used. The polarized Raman measurements were conducted using a polarizer in the scattered beam and a half-wave plate to rotate the scattered light polarization to optimize the gratings response.

**DFT Calculations.** Plane-wave DFT calculations were performed using the VASP package<sup>43</sup> equipped with the projector augmented-wave (PAW) method for electron–ion interactions. The local density approximation (LDA) was used for the exchange–correlation interaction with the energy cutoff set at 300 eV.<sup>18,23,44</sup> For bulk MoSe<sub>2</sub>, both atoms and cell volumes were allowed to relax until the residual forces were below 0.001 eV/Å. We used a  $24 \times 24 \times 4$  k-point sampling in the Monkhorst–Pack scheme for bulk calculations. Bilayer MoSe<sub>2</sub> systems were modeled in a periodic slab geometry using the optimized in-plane lattice constants of the bulk. For the five high-symmetry stacking configurations at 0° or 60° (Figure S12), a  $24 \times 24 \times 1$  k-point sampling was used since their in-plane lattice constants are the same as for the bulk ( $a = 3.25 \text{ Å}$ ). We also considered other twist angles with commensurate structures between 30° and 60° (i.e., periodic boundary conditions can be applied in the in-plane directions and a unit cell can be located), including 32.2°, 38.2°, 46.8°, 50.6°, and 52.7° (more details are given in Figure S13). For all systems, a vacuum region of at least 18 Å in the  $z$  direction normal to the plane was used to avoid spurious interactions with replicas, and all atoms were relaxed until the residual forces were below 0.001 eV/Å.

Phonon calculations were carried out using a finite difference scheme within the supercell approach. The Hellmann–Feynman forces in the supercell were computed by VASP for both positive and negative atomic displacements ( $\delta = 0.03 \text{ Å}$ ) and used in the PHONON software<sup>45</sup> to construct the dynamic matrix, whose diagonalization provides phonon frequencies and eigenvectors. Then nonresonant Raman intensity calculations were performed for some twist angles including 60° and 38.2°. For other angles, the systems were too large for the relatively costly Raman calculations.

The Raman intensity of a phonon mode is  $I \propto |e_i \cdot \tilde{R} \cdot e_s|^2$ , where  $e_i$  and  $e_s$  are the electric polarization vectors of the incident and scattered light, respectively, and  $\tilde{R}$  is the Raman tensor of the phonon mode. The matrix element of the ( $3 \times 3$ ) Raman tensor  $\tilde{R}$  of the  $j$ th phonon mode is given by<sup>46–48</sup>

$$\tilde{R}_{\alpha\beta}(j) = \sqrt{\frac{1}{\omega_j}} \sum_N \sum_l \sum_{\mu=1}^3 \frac{\partial \chi_{\alpha\beta}}{\partial r_l(\mu)} \frac{e_l^j(\mu)}{\sqrt{M_\mu}}$$

where  $\chi_{\alpha\beta} = (\epsilon_{\alpha\beta} - \delta_{\alpha\beta})/4\pi$  is the electric polarizability tensor related to the tensor of dielectric constant,  $\epsilon_{\alpha\beta}$ ,  $r_l(\mu)$  is the position of the  $\mu$ th atom along the direction  $l$ ,  $\frac{\partial \chi_{\alpha\beta}}{\partial r_l(\mu)}$  is the first derivative of the polarizability tensor (essentially the dielectric tensor) over the atomic displacement,  $e_l^j(\mu)$  is the displacement of the  $\mu$ th atom along the direction  $l$  in the  $j$ th phonon mode (the eigenvector of the dynamic matrix),  $\omega_j$  is the frequency of the  $j$ th phonon mode (its square is the eigenvalue of the dynamic matrix), and  $M_\mu$  is the mass of the  $\mu$ th atom.<sup>46</sup> To obtain Raman scattering, one needs to calculate derivatives of the dielectric constant tensors, in addition to the dynamic matrix discussed above. For both positive and negative atomic displacements in a single unit cell, the dielectric tensors were computed by VASP using density functional perturbation theory and then imported into PHONON to generate their derivatives (calculated by the finite difference approach). The Raman intensity for every phonon mode was obtained in the experimental backscattering configuration.

## ASSOCIATED CONTENT

### Supporting Information

The Supporting Information is available free of charge on the ACS Publications website at DOI: 10.1021/acsnano.5b07807.

Optical microscope and AFM images of typical MoSe<sub>2</sub> bilayer crystals; schematic representation of low- and high-frequency interlayer and intralayer Raman modes for bilayer MoSe<sub>2</sub>; comparison of LF Raman spectra acquired at different bilayer spots; polarized Raman measurements; high-frequency Raman spectra at different twist angles; LF Raman spectra for sample 2 and comparison of twist angle dependences for samples 1 and 2; schematics of five high-symmetry stacking patterns; atomic structures of bilayer MoSe<sub>2</sub> with  $\theta \neq 60^\circ$ ; commensurate and noncommensurate bilayer MoSe<sub>2</sub> systems for twist angles above 30°; DFT-calculated average interlayer separation, total energy, frequency, and Raman intensities of interlayer shear and breathing modes at different twist angles (PDF)

## AUTHOR INFORMATION

### Corresponding Author

\*E-mail: puretzky@ornl.gov.

### Author Contributions

<sup>†</sup>A. A. Puretzky and L. Liang contributed equally to this work.

### Notes

The authors declare no competing financial interest.

## ACKNOWLEDGMENTS

The Raman spectroscopy part of this research, including aspects of theory, was conducted at the Center for Nanophase Materials Sciences, a U.S. Department of Energy Office of Science User Facility. The synthesis science including CVD was supported by the U.S. Department of Energy, Office of Science, Basic Energy Sciences, Materials Sciences and Engineering Division. The theoretical work at Rensselaer Polytechnic Institute (RPI) was supported by NSF EFRI-2DARE 1542707. L.L. was supported by a Eugene P. Wigner Fellowship at the Oak Ridge National Laboratory. The computations were performed using the resources of the Center for Computational Innovation at RPI. This manuscript has been authored by UT-Battelle, LLC, under Contract No. DE-AC05-00OR22725 with the U.S. Department of Energy. The United States Government retains and the publisher, by accepting the article for publication, acknowledges that the United States Government retains a nonexclusive, paid-up, irrevocable, worldwide license to publish or reproduce the published form of this manuscript, or allow others to do so, for United States Government purposes. The Department of Energy will provide public access to these results of federally sponsored research in accordance with the DOE Public Access Plan (<http://energy.gov/downloads/doe-public-access-plan>).

## REFERENCES

- Geim, A. K.; Grigorieva, I. V. Van der Waals Heterostructures. *Nature* **2013**, *499*, 419–425.
- Hong, X. P.; Kim, J.; Shi, S. F.; Zhang, Y.; Jin, C. H.; Sun, Y. H.; Tongay, S.; Wu, J. Q.; Zhang, Y. F.; Wang, F. Ultrafast Charge Transfer in Atomically Thin MoS<sub>2</sub>/WS<sub>2</sub> Heterostructures. *Nat. Nanotechnol.* **2014**, *9*, 682–686.

- (3) Ceballos, F.; Bellus, M. Z.; Chiu, H. Y.; Zhao, H. Ultrafast Charge Separation and Indirect Exciton Formation in a MoS<sub>2</sub>-MoSe<sub>2</sub> van der Waals Heterostructure. *ACS Nano* **2014**, *8*, 12717–12724.
- (4) Rigosi, A. F.; Hill, H. M.; Li, Y. L.; Chernikov, A.; Heinz, T. F. Probing Interlayer Interactions in Transition Metal Dichalcogenide Heterostructures by Optical Spectroscopy: MoS<sub>2</sub>/WS<sub>2</sub> and MoSe<sub>2</sub>/WSe<sub>2</sub>. *Nano Lett.* **2015**, *15*, 5033–5038.
- (5) Kozawa, D.; Carvalho, A.; Verzhbitskiy, I.; Giustiniano, F.; Mouri, S.; Castro Neto, A. H.; Matsuda, K.; Eda, G. Efficient Interlayer Energy Transfer via 2D Dipole Coupling in MoSe<sub>2</sub>/WS<sub>2</sub> Heterostructures. *2015*, [Arxiv.org/pdf/1509.01875](https://arxiv.org/pdf/1509.01875).
- (6) Yu, Y. F.; Hu, S.; Su, L. Q.; Huang, L. J.; Liu, Y.; Jin, Z. H.; Puzetzy, A. A.; Geohegan, D. B.; Kim, K. W.; Zhang, Y.; Cao, L. Y. Equally Efficient Inter-Layer Exciton Relaxation and Improved Absorption in Epitaxial and Nonepitaxial MoS<sub>2</sub>/WS<sub>2</sub> Heterostructures. *Nano Lett.* **2015**, *15*, 486–491.
- (7) Rivera, P.; Schaibley, J. R.; Jones, A. M.; Ross, J. S.; Wu, S. F.; Aivazian, G.; Klement, P.; Seyler, K.; Clark, G.; Ghimire, N. J.; Yan, J. Q.; Mandrus, D. G.; Yao, W.; Xu, X. D. Observation of Long-Lived Interlayer Excitons in Monolayer MoSe<sub>2</sub>-WSe<sub>2</sub> Heterostructures. *Nat. Commun.* **2015**, *6*, 6242.
- (8) Heo, H.; Sung, J. H.; Cha, S.; Jang, B. G.; Kim, J. Y.; Jin, G.; Lee, D.; Ahn, J. H.; Lee, M. J.; Shim, J. H.; Choi, H.; Jo, M. H. Interlayer Orientation-Dependent Light Absorption and Emission in Monolayer Semiconductor Stacks. *Nat. Commun.* **2015**, *6*, 7372.
- (9) Lee, C. H.; Lee, G. H.; van der Zande, A. M.; Chen, W. C.; Li, Y. L.; Han, M. Y.; Cui, X.; Arefe, G.; Nuckolls, C.; Heinz, T. F.; Guo, J.; Hone, J.; Kim, P. Atomically Thin p-n Junctions with Van der Waals Heterointerfaces. *Nat. Nanotechnol.* **2014**, *9*, 676–681.
- (10) Fang, H.; Battaglia, C.; Carraro, C.; Nemsak, S.; Ozdol, B.; Kang, J. S.; Bechtel, H. A.; Desai, S. B.; Kronast, F.; Unal, A. A.; Conti, G.; Conlon, C.; Palsson, G. K.; Martin, M. C.; Minor, A. M.; Fadley, C. S.; Yablonovitch, E.; Maboudian, R.; Javey, A. Strong Interlayer Coupling in Van der Waals Heterostructures Built from Single-Layer Chalcogenides. *Proc. Natl. Acad. Sci. U. S. A.* **2014**, *111*, 6198–6202.
- (11) Gong, Y. J.; Lin, J. H.; Wang, X. L.; Shi, G.; Lei, S. D.; Lin, Z.; Zou, X. L.; Ye, G. L.; Vajtai, R.; Yakobson, B. I.; Terrones, H.; Terrones, M.; Tay, B. K.; Lou, J.; Pantelides, S. T.; Liu, Z.; Zhou, W.; Ajayan, P. M. Vertical and in-Plane Heterostructures from WS<sub>2</sub>/MoS<sub>2</sub> Monolayers. *Nat. Mater.* **2014**, *13*, 1135–1142.
- (12) Tongay, S.; Fan, W.; Kang, J.; Park, J.; Koldemir, U.; Suh, J.; Narang, D. S.; Liu, K.; Ji, J.; Li, J. B.; Sinclair, R.; Wu, J. Q. Tuning Interlayer Coupling in Large-Area Heterostructures with CVD-Grown MoS<sub>2</sub> and WS<sub>2</sub> Monolayers. *Nano Lett.* **2014**, *14*, 3185–3190.
- (13) Chiu, M. H.; Li, M. Y.; Zhang, W. J.; Hsu, W. T.; Chang, W. H.; Terrones, M.; Terrones, H.; Li, L. J. Spectroscopic Signatures for Interlayer Coupling in MoS<sub>2</sub>-WSe<sub>2</sub> Van der Waals Stacking. *ACS Nano* **2014**, *8*, 9649–9656.
- (14) Chiu, M. H.; Zhang, C. D.; Shiu, H. W.; Chuu, C. P.; Chen, C. H.; Chang, C. Y. S.; Chen, C. H.; Chou, M. Y.; Shih, C. K.; Li, L. J. Determination of Band Alignment in the Single-Layer MoS<sub>2</sub>/WSe<sub>2</sub> Heterojunction. *Nat. Commun.* **2015**, *6*, 7666.
- (15) Huang, S. X.; Ling, X.; Liang, L. B.; Kong, J.; Terrones, H.; Meunier, V.; Dresselhaus, M. S. Probing the Interlayer Coupling of Twisted Bilayer MoS<sub>2</sub> Using Photoluminescence Spectroscopy. *Nano Lett.* **2014**, *14*, 5500–5508.
- (16) Malard, L. M.; Alencar, T. V.; Barboza, A. P. M.; Mak, K. F.; de Paula, A. M. Observation of Intense Second Harmonic Generation from MoS<sub>2</sub> Atomic Crystals. *Phys. Rev. B: Condens. Matter Mater. Phys.* **2013**, *87*, 201401(R).
- (17) Van der Zande, A. M.; Kunstmann, J.; Chernikov, A.; Chenet, D. A.; You, Y. M.; Zhang, X. X.; Huang, P. Y.; Berkelbach, T. C.; Wang, L.; Zhang, F.; Hybertsen, M. S.; Muller, D. A.; Reichman, D. R.; Heinz, T. F.; Hone, J. C. Tailoring the Electronic Structure in Bilayer Molybdenum Disulfide via Interlayer Twist. *Nano Lett.* **2014**, *14*, 3869–3875.
- (18) Puzetzy, A. A.; Liang, L. B.; Li, X. F.; Xiao, K.; Wang, K.; Mahjouri-Samani, M.; Basile, L.; Idrobo, J. C.; Sumpter, B. G.; Meunier, V.; Geohegan, D. B. Low-Frequency Raman Fingerprints of Two-Dimensional Metal Dichalcogenide Layer Stacking Configurations. *ACS Nano* **2015**, *9*, 6333–6342.
- (19) Lui, C. H.; Ye, Z. P.; Ji, C.; Chiu, K. C.; Chou, C. T.; Andersen, T. I.; Means-Shively, C.; Anderson, H.; Wu, J. M.; Kidd, T.; Lee, Y. H.; He, R. Observation of Interlayer Phonon Modes in Van der Waals Heterostructures. *Phys. Rev. B: Condens. Matter Mater. Phys.* **2015**, *91*, 165403.
- (20) Lu, X.; Utama, M. I. B.; Lin, J. H.; Luo, X.; Zhao, Y. Y.; Zhang, J.; Pantelides, S. T.; Zhou, W.; Quek, S. Y.; Xiong, Q. H. Rapid and Nondestructive Identification of Polytypism and Stacking Sequences in Few-Layer Molybdenum Diselenide by Raman Spectroscopy. *Adv. Mater.* **2015**, *27*, 4502–4508.
- (21) Zeng, H. L.; Zhu, B. R.; Liu, K.; Fan, J. H.; Cui, X. D.; Zhang, Q. M. Low-Frequency Raman Modes and Electronic Excitations in Atomically thin MoS<sub>2</sub> Films. *Phys. Rev. B: Condens. Matter Mater. Phys.* **2012**, *86*, 241301.
- (22) Zhang, X.; Han, W. P.; Wu, J. B.; Milana, S.; Lu, Y.; Li, Q. Q.; Ferrari, A. C.; Tan, P. H. Raman Spectroscopy of Shear and Layer Breathing Modes in Multilayer MoS<sub>2</sub>. *Phys. Rev. B: Condens. Matter Mater. Phys.* **2013**, *87*, 115413.
- (23) Zhao, Y. Y.; Luo, X.; Li, H.; Zhang, J.; Araujo, P. T.; Gan, C. K.; Wu, J.; Zhang, H.; Quek, S. Y.; Dresselhaus, M. S.; Xiong, Q. H. Inter Layer Breathing and Shear Modes in Few-Trilayer MoS<sub>2</sub> and WSe<sub>2</sub>. *Nano Lett.* **2013**, *13*, 1007–1015.
- (24) Zhang, X.; Qiao, X. F.; Shi, W.; Wu, J. B.; Jiang, D. S.; Tan, P. H. Phonon and Raman Scattering of Two-Dimensional Transition Metal Dichalcogenides from Monolayer, Multilayer to Bulk Material. *Chem. Soc. Rev.* **2015**, *44*, 2757–2785.
- (25) Bhimanapati, G. R.; Lin, Z.; Meunier, V.; Jung, Y.; Cha, J.; Das, S.; Xiao, D.; Son, Y.; Strano, M. S.; Cooper, V. R.; et al. Recent Advances in Two-Dimensional Materials beyond Graphene. *ACS Nano* **2015**, *9*, 11509–11539.
- (26) Wu, J. B.; Zhang, X.; Ijas, M.; Han, W. P.; Qiao, X. F.; Li, X. L.; Jiang, D. S.; Ferrari, A. C.; Tan, P. H. Resonant Raman Spectroscopy of Twisted Multilayer Graphene. *Nat. Commun.* **2014**, *5*, 5309.
- (27) Tan, P. H.; Han, W. P.; Zhao, W. J.; Wu, Z. H.; Chang, K.; Wang, H.; Wang, Y. F.; Bonini, N.; Marzari, N.; Pugno, N.; Savini, G.; Lombardo, A.; Ferrari, A. C. The Shear Mode of Multilayer Graphene. *Nat. Mater.* **2012**, *11*, 294–300.
- (28) Lui, C. H.; Heinz, T. F. Measurement of Layer Breathing Mode Vibrations in Few-layer Graphene. *Phys. Rev. B: Condens. Matter Mater. Phys.* **2013**, *87*, 121404(R).
- (29) Ling, X.; Liang, L.; Huang, S.; Puzetzy, A. A.; Geohegan, D. B.; Sumpter, B. G.; Kong, J.; Meunier, V.; Dresselhaus, M. S. Low-Frequency Interlayer Breathing Modes in Few-Layer Black Phosphorus. *Nano Lett.* **2015**, *15*, 4080–4088.
- (30) Luo, X.; Lu, X.; Koon, G. K. W.; Castro Neto, A. H.; Özyilmaz, B.; Xiong, Q.; Quek, S. Y. Large Frequency Change with Thickness in Interlayer Breathing Mode-Significant Interlayer Interactions in Few Layer Black Phosphorus. *Nano Lett.* **2015**, *15*, 3931–3938.
- (31) Zhao, H.; Wu, J.; Zhong, H.; Guo, Q.; Wang, X.; Xia, F.; Yang, L.; Tan, P.; Wang, H. Interlayer Interactions in Anisotropic Atomically Thin Rhenium Diselenide. *Nano Res.* **2015**, *8*, 3651–3661.
- (32) Qiao, X.-F.; Wu, J.-B.; Zhou, L.-W.; Qiao, J.-S.; Shi, W.; Chen, T.; Zhang, X.; Zhang, J.; Ji, W.; Tan, P.-H. Polytypism and Unexpected Strong Interlayer Coupling of Two-Dimensional Layered ReS<sub>2</sub>. [ArXiv:1512.08935](https://arxiv.org/abs/1512.08935).
- (33) Zhao, Y.; Luo, X.; Zhang, J.; Wu, J.; Bai, X.; Wang, M.; Jia, J.; Peng, H.; Liu, Z.; Quek, S. Y.; Xiong, Q. Interlayer Vibrational Modes in Few-Quintuple-Layer Bi<sub>2</sub>Te<sub>3</sub> and Bi<sub>2</sub>Se<sub>3</sub> Two-Dimensional Crystals: Raman Spectroscopy and First-Principles Studies. *Phys. Rev. B: Condens. Matter Mater. Phys.* **2014**, *90*, 245428.
- (34) Cong, C.; Yu, T. Enhanced Ultra-Low-Frequency Interlayer Shear Modes in Folded Graphene Layers. *Nat. Commun.* **2014**, *5*, 4709.
- (35) Wu, J. B.; Hu, Z. X.; Zhang, X.; Han, W. P.; Lu, Y.; Shi, W.; Qiao, X. F.; Ijas, M.; Milana, S.; Ji, W.; Ferrari, A. C.; Tan, P. H. Interface Coupling in Twisted Multilayer Graphene by Resonant

Raman Spectroscopy of Layer Breathing Modes. *ACS Nano* **2015**, *9*, 7440–7449.

(36) Luo, X.; Lu, X.; Cong, C. X.; Yu, T.; Xiong, Q. H.; Quek, S. Y. Stacking Sequence Determines Raman Intensities of Observed Interlayer Shear Modes in 2D Layered Materials - A General Bond Polarizability Model. *Sci. Rep.* **2015**, *5*, 14565.

(37) O'Brien, M.; McEvoy, N.; Hanlon, D.; Hallam, T.; Coleman, J. N.; Duesberg, G. S. Mapping of Low-Frequency Raman Modes in CVD-Grown Transition Metal Dichalcogenides: Layer Number, Stacking Orientation and Resonant Effects. *Sci. Rep.* **2016**, *6*, 19476.

(38) Liu, K. H.; Zhang, L. M.; Cao, T.; Jin, C. H.; Qiu, D. A.; Zhou, Q.; Zettl, A.; Yang, P. D.; Louie, S. G.; Wang, F. Evolution of Interlayer Coupling in Twisted Molybdenum Disulfide Bilayers. *Nat. Commun.* **2014**, *5*, 4966.

(39) He, J. G.; Hummer, K.; Franchini, C. Stacking Effects on the Electronic and Optical Properties of Bilayer Transition Metal Dichalcogenides MoS<sub>2</sub>, MoSe<sub>2</sub>, WS<sub>2</sub>, and WSe<sub>2</sub>. *Phys. Rev. B: Condens. Matter Mater. Phys.* **2014**, *89*, 075409.

(40) Cao, B. X.; Li, T. S. Interlayer Electronic Coupling in Arbitrarily Stacked MoS<sub>2</sub> Bilayers Controlled by Interlayer S-S Interaction. *J. Phys. Chem. C* **2015**, *119*, 1247–1252.

(41) Boukhicha, M.; Calandra, M.; Measson, M. A.; Lancry, O.; Shukla, A. Anharmonic Phonons in Few-Layer MoS<sub>2</sub>: Raman Spectroscopy of Ultralow Energy Compression and Shear modes. *Phys. Rev. B: Condens. Matter Mater. Phys.* **2013**, *87*, 195316.

(42) Paulatto, L.; Mauri, F.; Lazzeri, M. Anharmonic Properties from a Generalized Third-Order *ab initio* Approach: Theory and Applications to Graphite and Graphene. *Phys. Rev. B: Condens. Matter Mater. Phys.* **2013**, *87*, 054304.

(43) Kresse, G.; Furthmüller, J. Efficiency of *ab-initio* Total Energy Calculations for Metals and Semiconductors Using a Plane-Wave Basis Set. *Comput. Mater. Sci.* **1996**, *6*, 15–50.

(44) Molina-Sanchez, A.; Wirtz, L. Phonons in Single-Layer and Few-Layer MoS<sub>2</sub> and WS<sub>2</sub>. *Phys. Rev. B: Condens. Matter Mater. Phys.* **2011**, *84*, 155413.

(45) Parlinski, K. *Computer Code PHONON*; Krakow, Poland, 2010.

(46) Liang, L. B.; Meunier, V. First-Principles Raman Spectra of MoS<sub>2</sub>, WS<sub>2</sub> and their Heterostructures. *Nanoscale* **2014**, *6*, 5394–5401.

(47) Umari, P.; Pasquarello, A.; Dal Corso, A. Raman Scattering Intensities in Alpha-Quartz: A First-Principles Investigation. *Phys. Rev. B: Condens. Matter Mater. Phys.* **2001**, *63*, 094305.

(48) Ceriotti, M.; Pietrucci, F.; Bernasconi, M. *Ab initio* Study of the Vibrational Properties of Crystalline TeO<sub>2</sub>: The Alpha, Beta, and Gamma Phases. *Phys. Rev. B: Condens. Matter Mater. Phys.* **2006**, *73*, 104304.